Hydrothermal vs. Electrochemical reduction of graphene oxide: a physicochemical and quartz crystal microbalance study

Caroline Keller, Gregory Barbillon, Catherine Debiemme-Chouvy, Ozlem Sel, Hubert Perrot

Hydrothermal vs. Electrochemical reduction of graphene oxide: a physico-chemical and quartz crystal microbalance study

Caroline Keller[a,*], Grégory Barbillon[a,b], Catherine Debiemme-Chouvy[a], Ozlem Sel[c,d], Hubert Perrot[a,**]

[a] Sorbonne Université, CNRS, Laboratoire Interfaces et Systèmes Electrochimiques, LISE, UMR 8235, 75005 Paris, France

[b] EPF – Engineering School, 55 avenue du Président Wilson, 94230 Cachan, France.

[c] Chimie du Solide et de l'Energie, UMR 8260, Collège de France, 75231 Paris, France

[d] Réseau sur le Stockage Electrochimique de l'Energie (RS2E), CNRS FR 3459, 33 Rue Saint Leu, 80039 Amiens Cedex, France

[*] Corresponding author.

[**] Corresponding author.

Email addresses caro-keller@orange.fr (Caroline Keller)
hubert.perrot@sorbonne-universite.fr (Hubert Perrot)

Keywords:

Reduced graphene oxide, hydrothermal reduction, electrochemical reduction, electrochemical impedance spectroscopy, electrochemical quartz crystal microbalance.

ABSTRACT

Reduced Graphene Oxide possesses numerous interesting properties, making it one of the most studied materials today. By this way, applications in various fields, including fundamental research, can be found. Nevertheless, the complexity of reduced Graphene Oxide lies in its fabrication process which defines their properties. In this paper, two fabrication methods -electrochemical and hydrothermal reduction of graphene oxide - were compared using physico-chemical and electrogravimetric analysis. Our findings reveal significant morphological differences between the two methods, accompanied by different electrochemical behaviors, when tested in aqueous electrolyte (i.e. 0.5 M Na_2SO_4). Specifically, electrochemically reduced graphene oxide exclusively involves

sodium (whether hydrated or not) in its charge compensation mechanism, whereas hydrothermally reduced graphene oxide also involves proton in sodium sulfate solution.

Graphical abstract

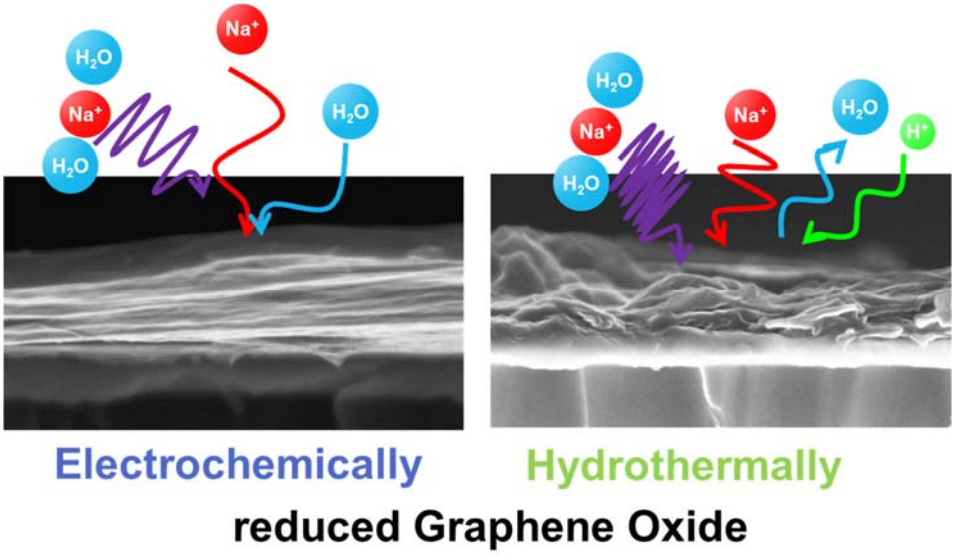

1. Introduction

Reduced Graphene Oxide (RGO) is a nanomaterial which properties offer a wide field of applications: supercapacitors, batteries, sensors, etc. Its special structure composed of graphene sheets allows for the adsorption of various components in between its layers. Its fabrication is achieved notably through the reduction of graphene oxide (GO), which can be done by many methods. The most common ones are thermal, hydrothermal, chemical and electrochemical reductions [1,2]. Studies have compared these methods and shown differences in oxygen content, surface functional groups and material structure [3–8]. The reduction method has a strong impact on the morphology, chemical composition and properties of the rGO [3,9]. One example is the study conducted by Yang *et al.* comparing chemically and thermally reduced graphene which showed "unfolded" and "stacked" structure, respectively [4].

Electrochemically reduced Graphene Oxide (**ERGO**) was demonstrated to have a stacked-film structure, with all the graphene layers superimposed like pages of a book [3,10]. This characteristic can be advantageous for it increases the density and therefore, the volumetric electrochemical energy density of this material. Unfortunately, π-stacking comes as a major drawback. Graphene layers agglomerate when dried, leading to a material with low-capacitive charge storage properties. To avoid this issue, several

studies have been proposed to control the drying process by lyophilization, ionic exchange or solvent exchange [5,10,11], or to add a spacer between graphene layers such as polydopamine or diamine [12–14]. Hydrothermally reduced Graphene Oxide (**HyRGO**) on its side is composed of bended graphene sheets, and allows a good dispersion of them to be obtained which is valuable for many applications [1,15]. This type of rGO was not reported to have π-stacking issues.

Hydrothermal and electrochemical reductions are the easiest and greenest ways to reduce graphene oxide, requiring few steps and no harsh chemicals. Hydrothermal reduction is simply done in water in a closed vessel at temperatures from 150 to 200°C [16]. As the reduced material is hydrophobic, organic solvents are often required to disperse them, but with additives such as ammonia, it is even possible to disperse HyRGO in water [1,15,17]. Electrochemical reduction is done by applying a cathodic current or potential to an electrode coated with GO in an aqueous electrolyte. None of these methods requires strong reductants nor high temperatures.

In this work, a series of physico-chemical characterizations including SEM and XPS were performed associated to classical electrochemical quartz microbalance (**EQCM**) in order to describe and understand the capacitive charge storage mechanisms in these materials. QCM is a widely used method which allows the mass deposited on the piezoelectric resonator, usually quartz, to be determined with a nanogram precision. In the context of this work, electroadsorption of ions happens during the charge compensation process [14] which leads to capacitive charge storage. To go further, ***ac*-electrogravimetry** was performed, a technique combining fast QCM and electrochemical impedance spectroscopy (**EIS**) to precisely separate the contribution of each species participating directly or indirectly in a charge compensation process. Key parameters can be extracted by this way : molar mass of the different ions involved as well as their kinetic and thermodynamic parameters [18]. This advanced technique has been widely used to study different kind of electrode materials such as carbon nanotubes [19] or rGO [14].

ERGO and HyRGO materials are different by their morphology and by their chemical composition. When testing their charge compensation mechanisms under an applied voltage, we demonstrate that for a given electrolyte, different mechanisms of electroadsorbed ions can be found despite both materials are rGO.

2. Experimental section

2.1. Materials preparation

Graphene Oxide (GO) was purchased from Merck as an aqueous suspension of 4 $mg.mL^{-1}$. For electrochemical reduction, it was diluted to 1 $mg.mL^{-1}$ and placed in an ultrasonic bath for 1 hour before 500µL was spray-coated on the gold electrode of an AT-cut quartz (AWSensors, Spain) working at 5 MHz (gold electrodes are 1 cm^2 for electrochemistry and 0.2 cm^2 for electrogravimetry) using a mask. This process was done on a plate heated at 200°C and maintained for 15 minutes to ensure a good water evaporation. ERGO film was obtained by applying a bias of -0.9 V *vs* Ag/AgCl for 5 minutes in a phosphate buffer solution, 0.1 M (100 mL of 0.1 M K_2HPO_4 mixed with 100 mL of 0.1 M KH_2PO_4). It was finally rinsed with ultrapure water and dried at room temperature overnight before any electrochemical testing. Pictures of the quartz coated with GO and ERGO are provided in Fig. S1.

For hydrothermal reduction, 8 mL of a 1 $mg.mL^{-1}$suspension of GO in water was placed in a closed reactor vessel with a 45 mL inner volume (Parr Instrument Company). The vessel was put in an oven at 170°C for 7 hours. After cooling, the black mixture was filtered and washed with water and ethanol, before being dispersed in N-methyl-2-pyrrolidone at a concentration of about 1 $mg.mL^{-1}$. Then, 500 µL of this mixture was put in ultrasonic bath for 1 hour before being spray-coated on the mask-protected gold electrode of an AT-cut quartz. The process was made on a heating plate kept at 250°C and the quartz crystal was let to rest on the heating plate for 15 minutes after the spray-drying. A picture of this quartz after coating is given on Fig. S1c.

For EQCM and *ac*-electrogravimetric measurements, ERGO and HyRGO mass loadings were 43 and 38 $\mu g.cm^{-2}$, respectively, while electrochemical geometric area was 1 cm^2 for both samples.

2.2. Physico-chemical characterizations

Field-emission-gun Scanning Electron Microscopy (FEG-SEM) was performed under a field emission gun scanning electron microscope (Ultra55, Zeiss) operating at 10 kV.

Contact Angle measurements were made with a Krüss DSA100 device and ADVANCE software. XPS analyses were performed using an Omicron Argus X-ray photoelectron

spectrometer, equipped with a monochromated Al source (Kα radiation, hν = 1486.6 eV). The emission of photoelectrons from the sample was analyzed at a photoelectron collection angle of 45° under ultra-high vacuum conditions (≤10^{-9} mBar). Spectra were carried out with a 100 eV pass energy for the survey scan and 20 eV pass energy for high resolution spectra. Binding energies were referenced to C 1s peak lowest energy maximum at 284.5 eV for ERGO and HyRGO and 285.0 eV for GO, assuming these maximums correspond to C=C and C-C, respectively. Element peak intensities were corrected by Scofield factors. The peak areas were determined after subtraction of a Shirley background. The spectra were fitted using Casa XPS software (Casa Software Ltd, U.K.) and applying a gaussian/lorentzian ratio equal to 70/30 for deconvolution. Raman spectroscopy was used to characterize the two types of samples. A Labram HR Evolution (Horiba) spectrophotometer was employed with a spectral resolution less than 2 cm^{-1} and an excitation wavelength of 532 nm. For all the Raman measurements, the laser power and the acquisition time have been set at 0.3 mW and 2 s, respectively. The excitation laser was focused with a microscope objective (×80; N.A.= 0.75), and this latter also enabled the collection of Raman signals from the samples.

2.3. Electrochemical and quartz crystal microbalance measurements

Electrochemical tests were done with a three-electrode cell configuration using a QCM cell from AWSensors. The reference electrode was a Mercury Sulfate Electrode (MSE), the counter electrode a 1 cm^2 platinum grid and the electrolyte Na_2SO_4 at a concentration of 0.5 M in ultrapure water. N_2 was bubbled in the electrolyte solution during 15 minutes before each electrochemical experiment to remove O_2. Sauerbrey equation was employed to convert the resonance frequency into areal mass:

$$\Delta m\ (g.cm^{-2}) = \frac{-\Delta f\ (Hz)}{C_S(Hz.g^{-1}.cm^2)} \quad (1)$$

with C_s = $16.95 \cdot 10^7$ $Hz.g^{-1}.cm^2$ for a 5 MHz working at 3rd overtone.

EQCM experiments were done with an Autolab potentiostat (PGSTAT 12), a lab-made oscillator and a Yokogawa frequency counter. Concomitant measurement of frequency and half-width-at-half-maximum (Γ) was performed by using an AWS-X1 equipment from AWSensors on 5 MHz quartz coupled with a Biologic SP200 potentiostat.

***A*c-electrogravimetry,** where *ac* stands for "alternative-current", combines fast QCM and electrochemical impedance spectroscopy (EIS). A four-channel frequency response analyzer (FRA, Solartron 1254) was connected to a homemade potentiostat. The quartz crystal was polarized at each chosen potential and a small amplitude sinusoidal variation ΔE (±70 mV) was added to the signal with frequencies of potential modulation from 63 kHz to 10 mHz. The response in current, ΔI, and in mass, Δm, were obtained after a numerical treatment of the collected data on the FRA and used for plotting four transfer functions (TF) in Nyquist representations: $\Delta E/\Delta I(\omega)$ (EIS), $\Delta q/\Delta E(\omega)$, $\Delta m/\Delta E(\omega)$ and $\Delta m/\Delta q(\omega)$ with q being the electrical charge. The fitting of these data was done thanks to a model detailed before [18]. Briefly, the model is based on the flux of ionic and solvent species, i, at the interface between the rGO thin film and the electrolyte (Fig. 1). The flux of ions and solvents, $J_i(C_i, E)$, going through this interface is considered to depend on two variables: the concentration of the species i, C_i, and the potential, E. It is expressed as follows:

$$\Delta J_i = \frac{\partial J_i}{\partial C_i}\Delta C_i + \frac{\partial J_i}{\partial E}\Delta E = K_i\,\Delta C_i + G_i \Delta E \tag{2}$$

where $K_i = \frac{\partial J_i}{\partial C_i}$ and $G_i = \frac{\partial J_i}{\partial E}$ denominated "kinetic constant" and "thermodynamic constant", respectively. Each experimental TF can be fitted with theoretical expressions involving a set of three parameters (K_i, G_i, M_i) for each species, i through:

$$\frac{\Delta E}{\Delta I}(\omega) = \frac{1}{j\omega d_f F\left(\frac{G_{c1}}{j\omega d_f + K_{c1}} + \frac{G_{c2}}{j\omega d_f + K_{c2}} + \frac{G_{c3}}{j\omega d_f + K_{c3}}\right) + \frac{1}{R_p + \frac{1}{j\omega C_p}}} \tag{3}$$

$$\frac{\Delta q}{\Delta E}(\omega) = d_f\left(\frac{G_{c1}}{j\omega d_f + K_{c1}} + \frac{G_{c2}}{j\omega d_f + K_{c2}} + \frac{G_{c3}}{j\omega d_f + K_{c3}}\right) \tag{4}$$

$$\frac{\Delta m}{\Delta E}(\omega) = -d_f\left(\frac{M_{c1}G_{c1}}{j\omega d_f + K_{c1}} + \frac{M_{c2}G_{c2}}{j\omega d_f + K_{c2}} + \frac{M_{c3}G_{c3}}{j\omega d_f + K_{c3}} + \frac{M_S G_S}{j\omega d_f + K_S}\right) \tag{5}$$

Where d_f is the film thickness, ω the pulsation ($\omega = 2\pi f$), F the Faradaic constant and R_p, C_p the parasitic resistance and capacity, respectively.

The relative concentration of each species can be estimated with Equation (6):

$$C_i - C_0 = \int_{E_0}^{E_1} \frac{\Delta C_i}{\Delta E}(\omega)\Big|_{\omega\to 0} = \int_{E_0}^{E_1} \frac{-G_i}{K_i} dE \tag{6}$$

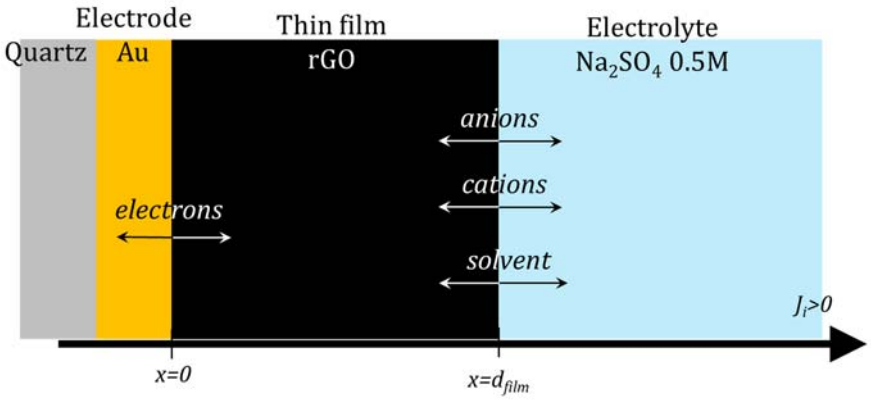

Fig. 1. Schematical view of the rGO (ERGO or HyRGO) thin film on gold electrode for describing the models for ac-electrogravimetric data fitting.

3. Results

3.1. Physico-chemical characterizations

Fig. 2 shows SEM micrographs of both materials, ERGO and HyRGO. With the aim of highlighting their differences, images (a) and (b) were made on samples with high-loading, which means that 3 times more GO/rGO was spray-dried on the substrate than for usual EQCM experiments (with final loadings of ~130 µg.cm^{-2}). With such high loading, their structural difference is obvious: while ERGO has many graphene sheets superimposed in a very ordered way, HyRGO is flaky and rough, as already reported in the literature [11,20]. While the same quantity of material was deposited on both samples, thicknesses were measured to 440 nm for ERGO and to 6 µm for HyRGO, involving a higher void/carbon ratio in HyRGO (based on 15 measurements on 7 different SEM images). Lower loadings, as shown in Fig. 2c and d, allow the density from the quartz crystal microbalance values to be estimated. They were found to be 2.2 g.cm^{-3} and 1.5 g.cm^{-3} for ERGO and HyRGO, respectively. RGO density is known to be close to 2.3 g.cm^{-3} [21,22], indicating that ERGO is a compact material while HyRGO has about 35 % voids in its structure. In these images, the same features as high loading samples are noticed: low roughness and aligned graphene layers for ERGO, while shallow roughness and imperfections in the stacking of the graphene layers for HyRGO. Even though both materials are spray-coated, strong morphological differences are observed are. GO is more flexible, moves and rearranges itself before and/or during its reduction to ERGO. HyRGO is ductile and stays as it was coated.

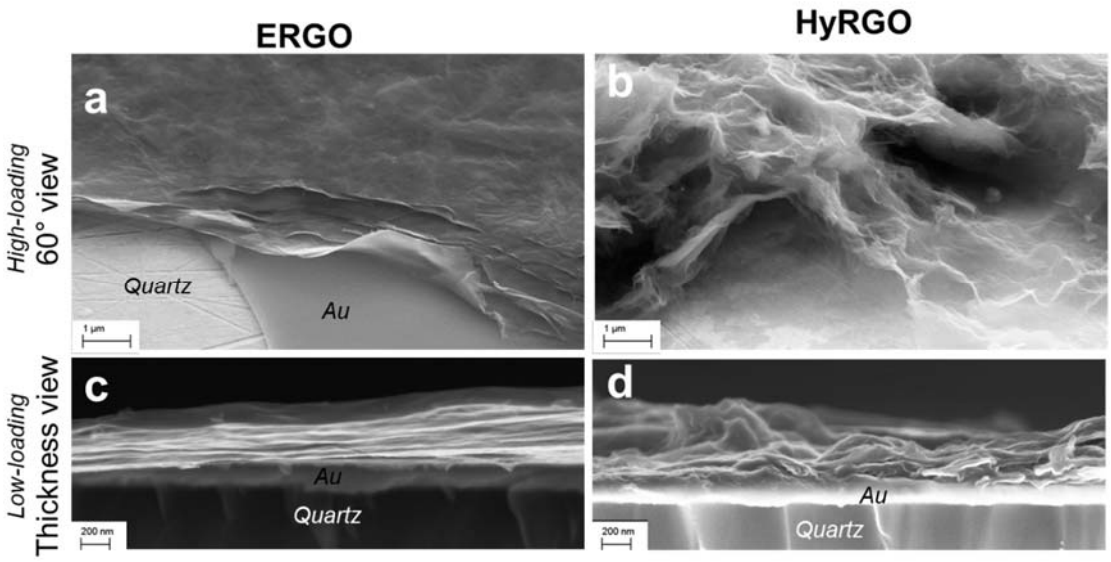

Fig. 2. SEM micrographs of rGO for (a,c) ERGO and (b,d) HyRGO. (a,b) for the high-loaded electrodes with a 60° view and (c,d) for the cross-section of the low-loaded electrode.

As to gain chemical information about the materials, X-ray Photoelectron Spectroscopy (XPS) was run on GO, ERGO and HyRGO. Survey spectra are presented in Fig. S3 and the quantifications in Table 1. The three samples mainly show C 1s and O 1s photopeaks, along with N 1s peak which is surprisingly present in the commercial GO (0.9 at. %). This sample also contains 1.1 at. % S as shown by S 2p peak, common for GO produced by the hard oxidation of graphite [23]. Once reduced, the C/O ratio increased from 2.3 to 6.1 and 5.7 for ERGO and HyRGO respectively, indicating a slightly better reduction of ERGO. Sulfur disappeared from the surface of both samples; nitrogen stays constant in ERGO but increases up to 3.2 at. % in HyRGO. This unexpected increase is probably linked to the use of N-methyl-2-pyrrolidone (NMP) as a solvent for the dispersion of HyRGO after its reduction. Either a little part of the solvent is still present in rGO, maybe in the pores, or it reacted during the drying step at 250°C and C-N bonds are integrated in the rGO. The use of this solvent was necessary for rGO dispersion, but the synthesis process of HyRGO can be optimized to disperse them in water [1,15,17].

Table 1. Atomic quantification from XPS of GO, ERGO and HyRGO.

At. %	C 1s	N 1s	O 1s	S 2p	C/O
GO	68.0	0.9	30.0	1.1	2.3
ERGO	85.2	0.8	14.0	0	6.1
HyRGO	82.4	3.2	14.5	0	5.7

Fig. 3 presents the XPS deconvolutions of C1s and O1s spectra, and areas are provided in Tables 2 and 3. Peak identification was done according to different references [24–28]. In HyRGO, C-O and C-N could not be separated, as their binding energies are close to 286 eV [25]. Therefore, C=O contribution coming from NMP was removed thanks to quantification considerations, and C 1s and O 1s deconvolution agreement was checked by computing the ratio between C=O/C-O in Table S1, explained in Note S1.

In agreement with the survey spectra, the ratio C/O increased in both ERGO and HyRGO films compared to GO (Table 1), confirming the good reduction of GO. Interestingly, the C-O contribution in GO is slightly different from the two other rGOs, as shown by different peak positions, indicating different chemical environments. After reduction, the main difference between ERGO and HyRGO stands in the C=O/C-O ratio. As seen in Fig. 3d and -f, C=O is predominant in HyRGO while C-O is in ERGO. From deconvolution results (with NMP contribution removed, see Note S1), the C=O/C-O ratio for HyRGO is twice the value of ERGO's (1 vs 0.5, Table S1 and Table 3). Hydrothermal reduction of GO therefore favors C-O reduction over C=O.

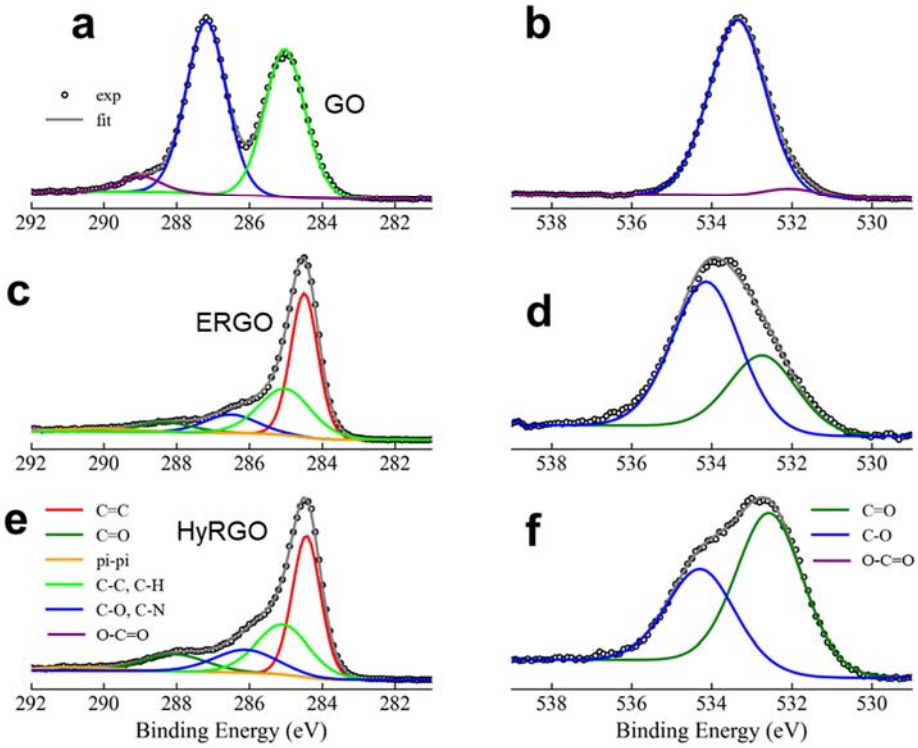

Fig. 3. XPS experimental spectra and deconvolution for GO (a-b), ERGO (c-d) and HYRGO (e-f). Details about peak positions are given in Table S2. (a,c,e: C1s ; b,d,f: O1s)

Table 2. Area integrated from the deconvolution of C 1s XPS spectra.

Area %	C=C	C-C, C-H	C-O / C-N	C=O	O=C-O	π-π
GO	0	44.0	51.3	0	4.7	0
ERGO	48.7	30.2	12.0	6.2	0	2.9
HyRGO	37.4	34.4	14.9	10.7	0	2.6

Table 3. Area integrated from the deconvolution of O 1s XPS spectra.

Area %	C-O	C=O
GO	94.8	5.2
ERGO	65.2	34.8
HyRGO	37.2	62.8

Finally, contact-angle measurement was run with water droplets (Fig. S2). ERGO has a contact angle of 57.9°, showing a hydrophilic behavior and HyRGO of 103.6°, showing a hydrophobic behavior. This difference raises questions, as C/O ratios are close for both materials (Table 1). Roughness alone cannot explain this phenomenon, as it can only straighten hydrophilicity (Wenzel model) or hydrophobicity (Cassie-Baxter model). Despite the fact that we heat HyRGO thin layer to 250°C for 15 minutes, XPS revealed 3 at.% of nitrogen which could come from NMP traces and therefore, increase rGO's hydrophobicity. Another explanation can be found in functional groups differences: HyRGO contains more C=O groups which were shown to increase hydrophobicity [29,30].

Fig. 4 displays the Raman spectra of ERGO and HyRGO. Several characteristic Raman bands are observed such D (1350 cm^{-1}), G (1594 cm^{-1}), 2D (2700 cm^{-1}), D+G (2944 cm^{-1}), and 2G (3188 cm^{-1}) bands. The G band is attributed to the first-order E_{2g} optical mode of graphene (or graphite) and the stretching mode from sp^2 carbon [31,32]. The D band is attributed to the disorder or defect band linked to the breathing mode of sp^2 carbon ring [31,32]. The 2D band corresponds to the overtone of the D band, the 2G band is assigned to the overtone of the G band, and the D+G band corresponds to the combined overtone of the D and G bands [32,33].

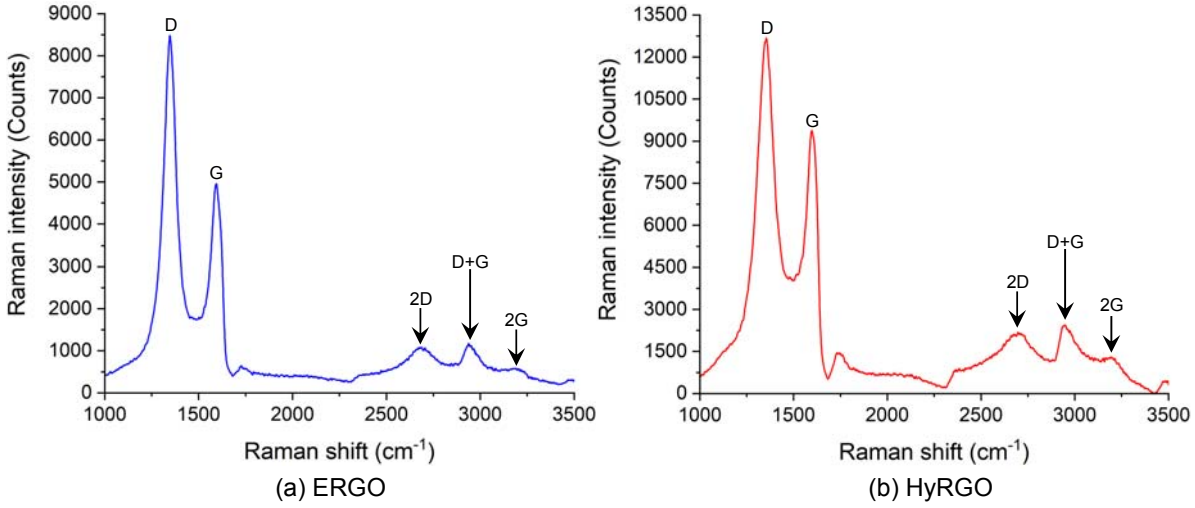

Fig. 4. Raman spectra of (a) ERGO and (b) HyRGO recorded at the excitation wavelength of 532 nm where D (1350 cm^{-1}), G (1594 cm^{-1}), 2D (2700 cm^{-1}), D+G (2944 cm^{-1}), and 2G (3188 cm^{-1}) bands are represented.

Next, we calculated the following intensity ratios I_D/I_G, I_{2D}/I_G, I_{2G}/I_D, I_{2G}/I_{D+G} and I_{D+G}/I_D in order to characterize the ERGO and HyRGO materials (see Table 4).

Table 4. Intensity ratios from Raman spectra of ERGO and HyRGO, and the crystallite size (L_a in nm) obtained from the values of I_D/I_G.

Samples	I_D/I_G	I_{2D}/I_G	I_{2G}/I_D	I_{2G}/I_{D+G}	I_{D+G}/I_D	L_a (nm)
ERGO	1.71	0.22	0.07	0.50	0.14	11.2
HyRGO	1.35	0.23	0.10	0.53	0.19	14.2

The I_D/I_G ratio is mainly used to evaluate the degree of quality (or structural disorder) in graphene or graphite layers as well as to estimate the mean crystallite size (mean size of crystalline (sp^2) clusters) [31,33]. The higher the I_D/I_G ratio, the higher the structural disorder (weaker quality). Thus, ERGO presents a higher disorder than HyRGO due to a larger value of the I_D/I_G ratio (see Table 4). For both ERGO and HyRGO, the values of the I_{2D}/I_G ratio are less than 1 indicating their multilayer nature (see Table 4) confirming the observations made by SEM (see Fig. 2). Indeed, the I_{2D}/I_G ratio is employed as indicator of the layer number for the graphene-type materials [34,35]. Furthermore, the values of the I_{2G}/I_D, I_{2G}/I_{D+G} and I_{D+G}/I_D ratios are weaker for ERGO than HyRGO indicating that the reduction degree is larger for ERGO than HyRGO as well as a lower electrical resistance for ERGO. Indeed, the weaker these ratios, the larger the reduction degree, the lower electrical resistance [32]. In addition, the crystallite size for ERGO is smaller than for HyRGO due to a larger structural disorder (more defects). The crystallite size (L_a in nm) is calculated with the following formula [33,36]:

$$L_a = (2.4 \times 10^{-10})\lambda_{exc}^4 \left(\frac{I_D}{I_G}\right)^{-1} \quad (7)$$

where λ_{exc} (in nm) corresponds to the excitation wavelength of the used laser.

As a summary of these physico-chemical characterizations, it was observed that ERGO and HyRGO have different morphologies as the first shows a parallel structure and the second a rougher morphology. Raman spectroscopy however evidenced for a better graphene quality for hydrothermal reduction, but at a lower reduction level, also highlighted by XPS results. XPS also showed a close C/O ratio for both materials but almost twice more C=O than C-O in HyRGO.

3.2. Classical Electrochemical Quartz Crystal Microbalance (EQCM)

Before any measurements, the validity of the Sauerbrey equation was checked. Fig. S4 shows frequency variation (Δf) as well as half-width-at-half-maximum (ΔΓ) during one CV cycle on the same graph, allowing them to be compared. In order to correctly use the Sauerbrey equation, the condition ΔΓ/-Δf < 10% should be respected, implying that the main frequency changes are indeed attributed to a mass change [37]. Fig. S4 shows that ΔΓ is evolving much less than Δf, with a maximum ratio of 10% between the two. This result implies that the major contribution to the frequency change is the mass change, and a minor contribution is related to other physico-chemical changes such as volume, density or stiffness changes. Another interesting feature of this plot is the opposite evolution of the two ΔΓ variations, indicating that the mechanism taking place during the charge compensation process is not the same for ERGO and HyRGO.

Fig. 5 presents the EQCM results based on cyclic voltammetry (Fig. 5a,c) and simultaneously mass responses of the electrodes (Fig. 5b,d) given by the QCM tool. In ERGO (Fig. 5-a), low scan-rate (10 mV·s^{-1}) shows a rectangular-like shape CV, which deforms and bends at higher scan rates. This behavior is attributed to electrode polarization resulting from kinetic limitations. At 10 mV·s^{-1}, ERGO electroadsorbs almost 2.5 wt. % of its initial mass when -0.95 V *vs.* MSE is applied, but this value decreases to 0.3 wt.% at 200 mV·s^{-1} (Fig. 5b).

HyRGO electrode behaves quite differently. Fig. 5c shows a rectangular-like shape from 10 to 200 mV·s^{-1}, which is not perfect indicating a possible pseudocapacitive behavior[38] that could be caused by carbonyl groups (which would be involved in quinones) or N-doping [39,40]. A zoom on the curves recorded at 50 mV·s^{-1} for both materials is provided in Fig. S5. Mass variations, presented in Fig. 5d, are slightly lower at 10 mV·s^{-1} than at higher scan rates. At 50, 100 and 200 mV·s^{-1}, Δm has a similar behavior going up to 4 wt. % electroadsorbed mass at -0.95 V *vs.* MSE with low hysteresis, indicating fast kinetics.

Capacity of both materials was computed at 50 mV·s^{-1}, because the current response has a rectangular shape for both materials at this scan rate, through:

$$C\ [F \cdot g^{-1}] = \frac{\int I\, dV}{2\, v\, \Delta V\, m} \quad (8)$$

with *I* the current, *v* the scan rate, *ΔV* the potential window and *m* the mass of the film. Capacities at 50 mV·s^{-1} were found close: 43.6 F·g^{-1} and 41.9 F·g^{-1} for ERGO and HyRGO, respectively. Fig. 6-a show that their evolution follows opposite paths: while ERGO loses more than half of its capacity from 50 to 200 mV·s^{-1}, HyRGO maintains stable and even gain 20% capacity between 50 and 100 mV·s^{-1}, probably associated to electrochemical activation.

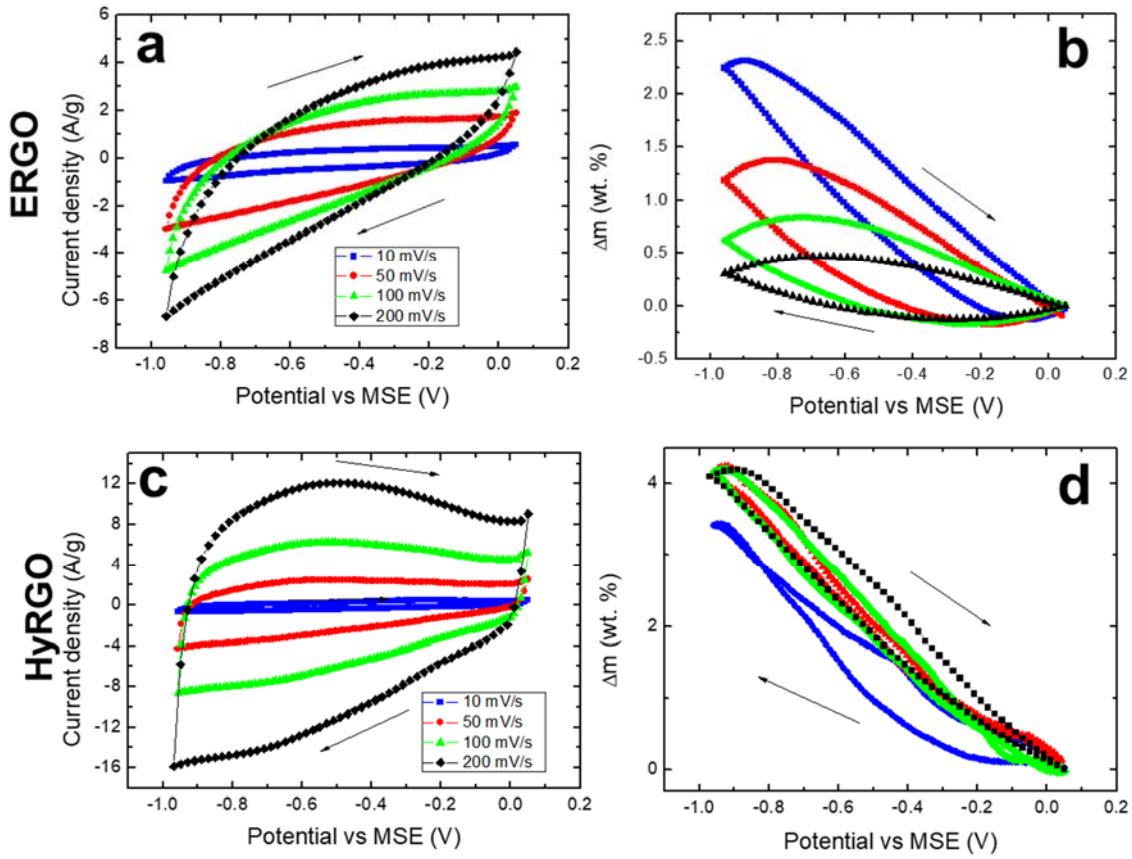

Fig. 5. EQCM results for ERGO (a-b) and HyRGO (c-d): Current density (a,c), and mass variation (b,d) *vs.* applied potential. Electrolyte is Na_2SO_4 0.5 M.

Fig. 6-b presents the mass per electron (MPE) vs. the applied potential for cathodic currents at 10 mV·s^{-1}. MPE is computed by a combination between current and gravimetric results through this relationship:

$$MPE\ [g.mol^{-1}] = F\frac{\Delta m}{\Delta q} = F\frac{\Delta m}{\Delta E}\frac{\Delta E}{\Delta t}\frac{\Delta t}{\Delta q} = \frac{F\ [A.s.mol^{-1}]\cdot v\ [V.s^{-1}]}{i\ [A.cm^{-2}]}\cdot\frac{\Delta m\ [g.cm^{-2}]}{\Delta E\ [V]} \quad (9)$$

MPE gives an idea about the mean molar mass of species electroadsorbed during the charge compensation process. For ERGO, a |MPE| value between 50 and 70 g.mol^{-1} is

computed, which could correspond to sodium in an hydrated form or simply followed by water molecules ($Na^+ + 2H_2O$: 59 g.mol^{-1}). For HyRGO, this value is slightly higher, it varies between 60 and 120 g.mol^{-1}, also corresponding to sodium and water molecules.

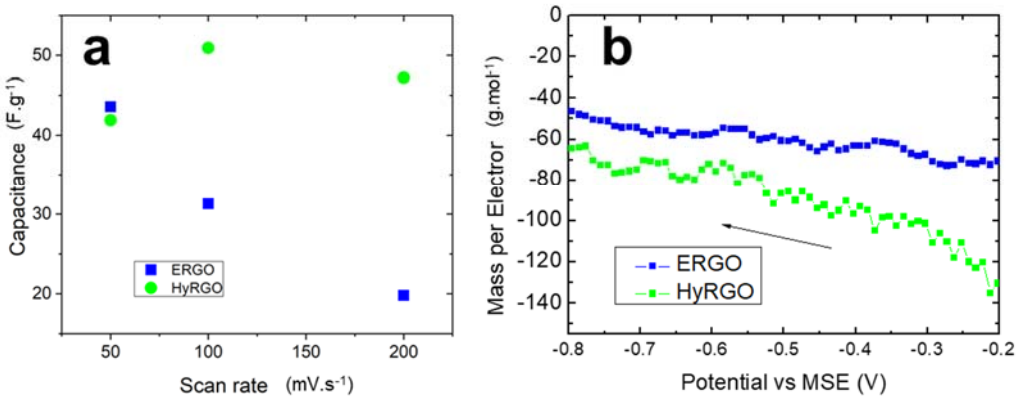

Fig. 6. (a) Capacity evolution compared to scan rate and (b) Mass per Electron (MPE) exchanged as a function of potential, at 10 mV·s^{-1}, calculated from cathodic current, in Na_2SO_4 0.5 M.

Despite ERGO and HyRGO have similar capacities, ERGO shows a slow charge storage behavior while HyRGO is quicker and has pseudo-capacitance, probably related to its oxygen and nitrogen- functional groups identified in XPS. MPE has evidenced that a mix of species participates the charge storage mechanisms in both rGO, but a more advanced technique is required to decipher on the nature of these species.

3.3. *Ac*-electrogravimetry

To go deeper in the understanding of the charge compensation mechanism, *ac*-electrogravimetric experiments were conducted. *Ac*-electrogravimetry is a combination of fast QCM and EIS which allows to discriminate the species that participate to the interfacial charge compensation process. Four transfer functions (TF) are plotted from the data acquisition: $\Delta E/\Delta I(\omega)$, $\Delta q/\Delta E(\omega)$, $\Delta m/\Delta E(\omega)$ and $\Delta m/\Delta q(\omega)$. Complementary transfer functions are checked to improve the modeling precision, removing the contribution of one cation or anion, called partial transfer functions [41]. A set of three parameters needs to be fitted for each contributing species: (M_i, K_i, G_i) with M_i being the molar mass of species i, K_i its kinetic constant and G_i its thermodynamic constant (see Equation (2)). Results of this fit are plotted in Fig. 7 for -0.5 V vs MSE, and additional TF and the corresponding fits of this dataset are provided in Fig. S6.

EIS is presented in Fig. 7a and a zoom on the response at high frequency is provided in Fig. S7. Electrolyte resistance, R_{el}, measured as the starting point of EIS, *ie* at high frequencies, is measured at 29 Ω.cm² for HyRGO and 14 Ω.cm² for ERGO. The higher electrolyte resistance for HyRGO can be explained by its hydrophobicity, but also by the higher HyRGO porosity. Impedance values are indeed presented in Ω.cm² and computed with rGO geometric area (1 cm²) but their developed area is different. Considering a higher developed area for HyRGO is therefore coherent with the higher measured electrolyte resistance.

$\Delta q/\Delta E(\omega)$ TFs presented in Fig. 7b show two different behaviors: while ERGO has only one loop, HyRGO has two, indicating that at least two species participate the charge compensation processes with different kinetic constants. HyRGO's second loop has maxima at 10 mHz, a low frequency which could be related to a reversible faradic process. Looking at HyRGO's first loop gives an indication about the total capacity of this material: as its diameter is larger than ERGO's, its full capacity is also bigger. This is coherent with the SEM observations where HyRGO seemed to have more porosity than ERGO.

With the quantitative *ac*-electrogravimetry fitting presented in Fig. 7, we could conclude that two cations and free solvent molecules are involved in ERGO charge compensation mechanism: $Na^+.2H_2O$, Na^+ and H_2O, the latter accompanying the cations. For HyRGO, $Na^+.2H_2O$ and Na^+ are also found but another loop appears at low frequencies in $\Delta q/\Delta E(\omega)$ TF (Fig. 7b) and in the fourth quadrant of $\Delta m/\Delta E(\omega)$ TF (Fig. 7d). These loops are well fitted with H^+ contribution and H_2O in the reverse flux direction. We tried to fit with anion OH^- going in the anion direction but the partial derivative did not match; we concluded that H^+ and opposite H_2O flux are happening at low frequencies in this HyRGO layer.

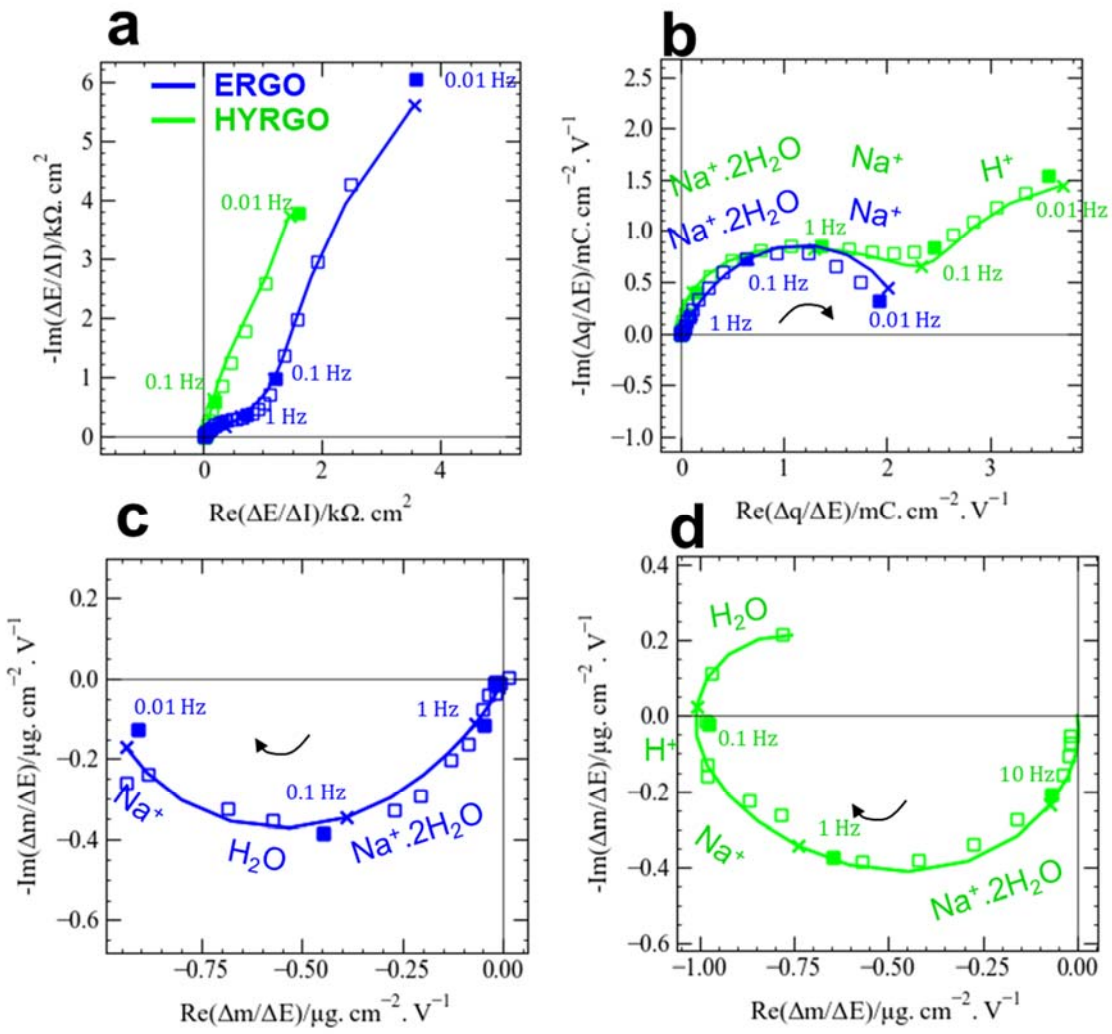

Fig. 7. *Ac*-electrogravimetric results, experimental (squares) and theoretical (lines) curves. Measurement at -0.5 V vs. MSE in Na_2SO_4 0.5 M. (a) ΔE/ΔI(ω), (b) Δq/ΔE(ω), (c) Δm/ΔE(ω) of ERGO and (d) Δm/ΔE(ω) of HyRGO.

Fig. 8a presents a comparison of *ac*-electrogravimetric parameters for ERGO and HyRGO. Their evolution as a function of the potential is given in Fig. S9. The kinetic parameter, K_i, is higher for the cations in HyRGO compared to ERGO, in agreement with the fastest kinetics observed in Fig. 5. Water is slower in HyRGO than ERGO, but it is also going in opposite direction: in HyRGO, water molecules flux is reverse to the cationic sense, explaining why they are slower in this sample. Comparing the ions together, the fastest cation is always the hydrated sodium, in agreement with our previous studies [42,43]. R_{ti} parameters are computed from the G_i parameter following $-1/(F.G_i)$, F being the Faraday

constant, and is analogous to a charge transfer resistance. R_{ti} follows K_i's tendency: the higher the K_i, the lower the R_t.

Fig. 8-b and c present the evolution of the concentration for each ions, computed with Equation 6. It shows that the prominent ions are not the fastest ones; Na^+ is indeed the predominant cation for ERGO, and H^+ is for HyRGO.

Thanks to this concentration variation computation, the classical gravimetric cyclic voltammetry could be reconstructed as presented in Fig. S8. For ERGO, we could only perform *ac*-electrogravimetry measurements at three different potentials because the sample degrades too quickly. For HyRGO, the data acquired at 10 $mV \cdot s^{-1}$ could not be reconstructed but 1 $mV \cdot s^{-1}$ could. Cycling at lower scan rates involves all the species in the charge compensation process, including the slow water flux and therefore allows a better fit with *ac*-electrogravimetric results to be obtained. For both materials, the fitting obtained from experimental ac-electrogravimetry agrees well with the former EQCM experiments.

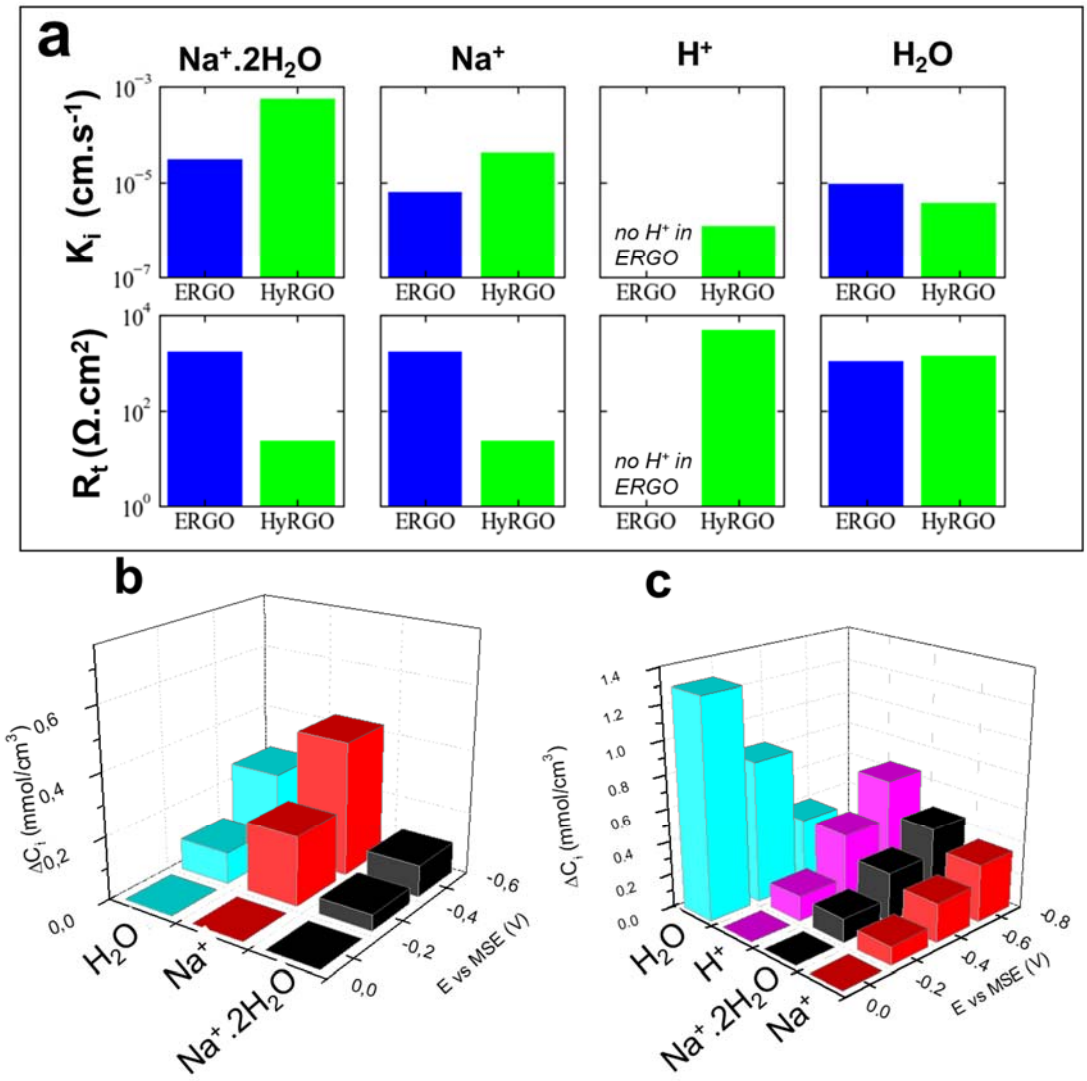

Fig. 8. (a) Comparison of the K_i and R_i (-1/(FG_i)) parameters for ERGO and HyRGO at -0.5 V vs MSE. Variation of concentrations of the species as a function of applied potential for (b) ERGO and (c) HyRGO.

4. Discussion

SEM observations have shown that ERGO has well-ordered graphene layers. Despite its hydrophilicity, charge compensation mechanism is slow, as demonstrated by *ac*-electrogravimetric measurements. As ERGO was tested every day in our laboratory, it was found unstable: after being dried, the next electrochemical test presented low current and mass responses, probed by EQCM. This phenomena is attributed to π-stacking which was already observed for ERGO materials [11] and certainly favored by the good alignment of its graphene layers. Ions slowness in the charge compensation process could also be

caused by ERGO's morphology: as illustrated in Fig. 9-a, few transversal pores caused by the well-ordered structure leads to less path for charge compensation process, causing "traffic jam" in the layer. Despite having a lower electrical resistance as evidenced by Raman spectroscopy (i.e. weaker $I_{2G}/I_{D,}$ I_{2G}/I_{D+G} and I_{D+G}/I_D ratios [32]), ERGO ions storage is slow, evidencing for a mechanistic issue rather than a chemical issue. Small pores, resulting from π-stacking, induce few bigger ions electroadsorbed, as shown by the low concentration of $Na^+.2H_2O$ in ERGO in Fig. 8c. Smaller ions such as Na^+ can enter the small pores but are slowed down by the low transversal pores leading through the ERGO layer. Their desolvation also costs energy and time. Free water molecules are slowly electro-dragged by cations as already observed in previous works [14,42].

HyRGO did not show this π-stacking stability issue: we could dry it and test it as many times as we want, the same current and mass changes were obtained at every cycle. We believe that its structure can explain this property: bended rigid graphene sheets make it less easy to π-stack between two sheets. The presence of C=O functions could also reduce this tendency. The more chaotic structure of this graphene sheets also creates bigger pores and more pathways for ions, explaining the fastest speed of charge compensation processes and the highest concentration of bigger ions (Fig. 8b). *Ac*-electrogravimetry revealed that H^+ is electroadsorbed at the same time than water's expulsion, at low frequencies. This oxonium ion dissociation is illustrated in Fig. 9b and could be explained by two reasons: i) the main chemical difference with ERGO is the highest presence of C=O groups at the surface of HyRGO along with nitrogen presence, which are both known to belong to groups reduced with the help of H^+ [39,40], and ii) HyRGO's graphene layers have more edges than ERGO, which could be sites favoring H_3O^+ dissociation in H^+ and H_2O. H^+ participation to electrochemical processes in a neutral electrolyte was already observed in previous works; H^+ comes from aqueous electrolyte and leads to local pH changes [19,44]. As for cation electron-dragging, anionic electro-dragging of water as observed in this sample was also already characterized in previous studies [45,46].

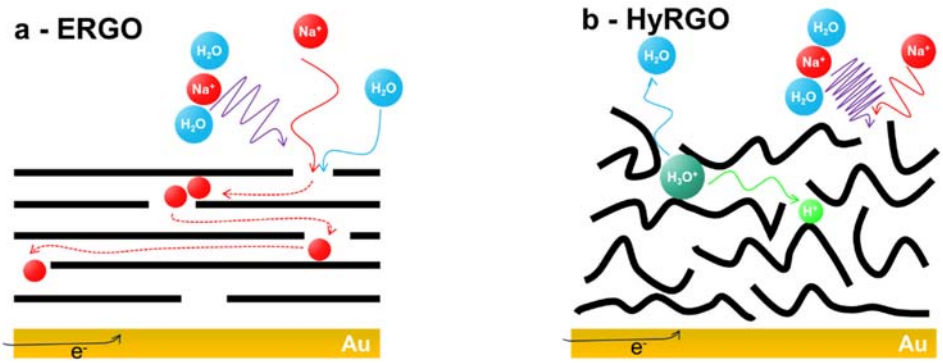

Fig. 9. Proposed electroadsorption mechanisms happening in ERGO (a) and HyRGO (b).

5. Conclusions

In this work two reduction methods of graphene oxide were compared, leading to two different reduced graphene oxide materials. Despite its hydrophilic behavior, ERGO is a slow capacitive material because of its high π-stacking. In order to use it as a supercapacitive electrode, priority number one is to fight the π-stacking. Many ways are already on work such as nanopillars or solvent exchange [10,13,47]. The second priority is to create transversal pores. This can be done by rethinking the cell geometry (interdigitated electrodes allow to avoid this issue) or by structuring them in a chemical or physical way.

Charge storage in HyRGO is faster, but even with its high stability, its capacity is low compared to the theoretical value for graphene. This means that an intrinsic π-stacking is present in HyRGO, happening during the reduction process. Working on hydrophilicity of such materials could improve their performances, besides removing the dispersion step in an organic solvent. This can be done by increasing the pH during the reduction process [15]. Another interesting feature is the electroadsorption of H^+ in the charge compensation process, even in neutral electrolyte. This can cause issues in reactivity and local change of pH which could be detrimental to the device and electrolyte additives but can be an advantage depending on the application aimed at. For example, a low local pH can favor the water reduction reaction which can be an asset for water electrolysis.

Summarizing, rGOs are a family composed of different materials. Graphene Oxide reduction method should be carefully chosen accordingly to the desired properties. Studying the influence of the starting GO material and especially its functional groups on the resulting rGO could be of high interest; such as the numerous possibilities for its

reduction, its fabrication process can also follow several synthetic routes [48]. As demonstrated in this study, rGO physico-chemical properties have a high impact on its electrochemical behavior, again evidencing for the high sensitivity of carbon materials surfaces to their processing conditions.

Credit authorship contribution statement

Conceptualization by CK, HP and OS ; Data curation by CK ; Formal analysis by CK, GB, CDC, HP and OS ; Funding acquisition by HP and OS ; Investigation by CK, GB, HP and OS ; Methodology by CK, HP and OS ; Project administration by HP and OS ; Resources by HP and OS ; Supervision by HP and OS ; Validation by HP, GB, OS and CDC ; Visualization by CK ; Writing - original draft by CK ; and Writing - review & editing by CK, GB, HP, CDC and OS.

Declaration of competing interest

The authors declare no competing interest.

Acknowledgements

The authors would like to thank Françoise Pillier and Stéphanie Delbrel for FEG-SEM measurements and Antoine Miche for XPS measurements. CK, HP and OS also acknowledge ANR MoveYourIon (ANR-19-CE06/0025) funded by the French "Agence Nationale de la Recherche" for financing.

References

[1] S. Pei, H.-M. Cheng, The reduction of graphene oxide, Carbon 50 (2012) 3210–3228. https://doi.org/10.1016/j.carbon.2011.11.010.

[2] B. Qi, K. Ren, Y. Lin, S. Zhang, T. Wei, Z. Fan, Design of layered-stacking graphene assemblies as advanced electrodes for supercapacitors, Particuology 60 (2022) 1–13. https://doi.org/10.1016/j.partic.2021.03.001.

[3] Y. Shang, D. Zhang, Y. Liu, C. Guo, Preliminary comparison of different reduction methods of graphene oxide, Bull. Mater. Sci. 38 (2015) 7–12. https://doi.org/10.1007/s12034-014-0794-7.

[4] J. Yang, J. Wang, Y. Tang, D. Wang, X. Li, Y. Hu, R. Li, G. Liang, T.-K. Sham, X. Sun, LiFePO4–graphene as a superior cathode material for rechargeable lithium batteries: impact of stacked graphene and unfolded graphene, Energy Environ. Sci. 6 (2013) 1521–1528. https://doi.org/10.1039/C3EE24163G.

[5] Y. Yoon, K. Lee, C. Baik, H. Yoo, M. Min, Y. Park, S.M. Lee, H. Lee, Anti-Solvent Derived Non-Stacked Reduced Graphene Oxide for High Performance Supercapacitors, Adv. Mater. 25 (2013) 4437–4444. https://doi.org/10.1002/adma.201301230.
[6] M.P. Lavin-Lopez, A. Paton-Carrero, L. Sanchez-Silva, J.L. Valverde, A. Romero, Influence of the reduction strategy in the synthesis of reduced graphene oxide, Adv. Powder Technol. 28 (2017) 3195–3203. https://doi.org/10.1016/j.apt.2017.09.032.
[7] P.P.A. Jose, M.S. Kala, N. Kalarikkal, S. Thomas, Reduced graphene oxide produced by chemical and hydrothermal methods, Mater. Today Proc. 5 (2018) 16306–16312. https://doi.org/10.1016/j.matpr.2018.05.124.
[8] H.A. Becerril, J. Mao, Z. Liu, R.M. Stoltenberg, Z. Bao, Y. Chen, Evaluation of Solution-Processed Reduced Graphene Oxide Films as Transparent Conductors, ACS Nano 2 (2008) 463–470. https://doi.org/10.1021/nn700375n.
[9] X. Xiang, Y. Zhu, C. Gao, H. Du, C. Guo, Study on the structure of reduced graphene oxide prepared by different reduction methods, Carbon Lett. 32 (2022) 557–566. https://doi.org/10.1007/s42823-021-00287-6.
[10] Y. Chen, K. Chen, H. Bai, L. Li, Electrochemically reduced graphene porous material as light absorber for light-driven thermoelectric generator, J. Mater. Chem. 22 (2012) 17800–17804. https://doi.org/10.1039/C2JM33530A.
[11] A. Zhou, J. Bai, W. Hong, H. Bai, Electrochemically reduced graphene oxide: Preparation, composites, and applications, Carbon 191 (2022) 301–332. https://doi.org/10.1016/j.carbon.2022.01.056.
[12] H. Banda, S. Périé, B. Daffos, P.-L. Taberna, L. Dubois, O. Crosnier, P. Simon, D. Lee, G. De Paëpe, F. Duclairoir, Sparsely Pillared Graphene Materials for High-Performance Supercapacitors: Improving Ion Transport and Storage Capacity, ACS Nano 13 (2019) 1443–1453. https://doi.org/10.1021/acsnano.8b07102.
[13] A. Bouzina, H. Perrot, O. Sel, C. Debiemme-Chouvy, Preventing Graphene from Restacking via Bioinspired Chemical Inserts: Toward a Superior 2D Micro-supercapacitor Electrode, ACS Appl. Nano Mater. 4 (2021) 4964–4973. https://doi.org/10.1021/acsanm.1c00489.
[14] A. Bouzina, R. Meng, C. Bazin, H. Perrot, O. Sel, C. Debiemme-Chouvy, Highly Ordered Graphene Polydopamine Composite Allowing Fast Motion of Cations: Toward a High-Performance Microsupercapacitor, Adv. Mater. Interfaces 10 (2023) 2300442. https://doi.org/10.1002/admi.202300442.
[15] Y. Zhou, Q. Bao, L.A.L. Tang, Y. Zhong, K.P. Loh, Hydrothermal Dehydration for the "Green" Reduction of Exfoliated Graphene Oxide to Graphene and Demonstration of Tunable Optical Limiting Properties, Chem. Mater. 21 (2009) 2950–2956. https://doi.org/10.1021/cm9006603.
[16] Y. Zhao, C. Li, X. Fan, J. Wang, G. Yuan, X. Song, J. Chen, Z. Li, Study on the separation performance of the multi-channel reduced graphene oxide membranes, Appl. Surf. Sci. 384 (2016) 279–286. https://doi.org/10.1016/j.apsusc.2016.05.036.
[17] J.N. Ding, Y.B. Liu, N.Y. Yuan, G.Q. Ding, Y. Fan, C.T. Yu, The influence of temperature, time and concentration on the dispersion of reduced graphene oxide prepared by hydrothermal reduction, Diam. Relat. Mater. 21 (2012) 11–15. https://doi.org/10.1016/j.diamond.2011.08.004.
[18] C. Gabrielli, J.J. García-Jareño, M. Keddam, H. Perrot, F. Vicente, Ac-Electrogravimetry Study of Electroactive Thin Films. I. Application to Prussian Blue, J. Phys. Chem. B 106 (2002) 3182–3191. https://doi.org/10.1021/jp013924x.
[19] F. Escobar-Teran, H. Perrot, O. Sel, Ion Dynamics at the Carbon Electrode/Electrolyte Interface: Influence of Carbon Nanotubes Types, Materials 15 (2022) 1867. https://doi.org/10.3390/ma15051867.
[20] Y. Xu, K. Sheng, C. Li, G. Shi, Self-Assembled Graphene Hydrogel via a One-Step Hydrothermal Process, ACS Nano 4 (2010) 4324–4330. https://doi.org/10.1021/nn101187z.
[21] L. Torrisi, M. Cutroneo, A. Torrisi, L. Silipigni, Measurements on Five Characterizing Properties of Graphene Oxide and Reduced Graphene Oxide Foils, Phys. Status Solidi A 219 (2022) 2100628. https://doi.org/10.1002/pssa.202100628.

[22] J. Zhong, W. Sun, Q. Wei, X. Qian, H.-M. Cheng, W. Ren, Efficient and scalable synthesis of highly aligned and compact two-dimensional nanosheet films with record performances, Nat. Commun. 9 (2018) 3484. https://doi.org/10.1038/s41467-018-05723-2.
[23] A.G. Bannov, A.A. Timofeeva, V.V. Shinkarev, K.D. Dyukova, A.V. Ukhina, E.A. Maksimovskii, S.I. Yusin, Synthesis and studies of properties of graphite oxide and thermally expanded graphite, Prot. Met. Phys. Chem. Surf. 50 (2014) 183–190. https://doi.org/10.1134/S207020511402004X.
[24] M.C. Biesinger, Accessing the robustness of adventitious carbon for charge referencing (correction) purposes in XPS analysis: Insights from a multi-user facility data review, Appl. Surf. Sci. 597 (2022) 153681. https://doi.org/10.1016/j.apsusc.2022.153681.
[25] M.K. Rabchinskii, S.D. Saveliev, D.Yu. Stolyarova, M. Brzhezinskaya, D.A. Kirilenko, M.V. Baidakova, S.A. Ryzhkov, V.V. Shnitov, V.V. Sysoev, P.N. Brunkov, Modulating nitrogen species via N-doping and post annealing of graphene derivatives: XPS and XAS examination, Carbon 182 (2021) 593–604. https://doi.org/10.1016/j.carbon.2021.06.057.
[26] R. Al-Gaashani, A. Najjar, Y. Zakaria, S. Mansour, M.A. Atieh, XPS and structural studies of high quality graphene oxide and reduced graphene oxide prepared by different chemical oxidation methods, Ceram. Int. 45 (2019) 14439–14448. https://doi.org/10.1016/j.ceramint.2019.04.165.
[27] L. Stobinski, B. Lesiak, A. Malolepszy, M. Mazurkiewicz, B. Mierzwa, J. Zemek, P. Jiricek, I. Bieloshapka, Graphene oxide and reduced graphene oxide studied by the XRD, TEM and electron spectroscopy methods, J. Electron Spectrosc. Relat. Phenom. 195 (2014) 145–154. https://doi.org/10.1016/j.elspec.2014.07.003.
[28] J.C. Fuggle, L.M. Watson, D.J. Fabian, S. Affrossman, X-ray photoelectron studies of the reaction of clean metals (Mg, Al, Cr, Mn) with oxygen and water vapour, Surf. Sci. 49 (1975) 61–76. https://doi.org/10.1016/0039-6028(75)90328-3.
[29] M. Matsuguchi, S. Umeda, Y. Sadaoka, Y. Sakai, Characterization of polymers for a capacitive-type humidity sensor based on water sorption behavior, Sens. Actuators B Chem. 49 (1998) 179–185. https://doi.org/10.1016/S0925-4005(98)00117-8.
[30] Y. Zhang, X. Jing, K. Jing, L. Chang, W. Bao, Study on the pore structure and oxygen-containing functional groups devoting to the hydrophilic force of dewatered lignite, Appl. Surf. Sci. 324 (2015) 90–98. https://doi.org/10.1016/j.apsusc.2014.10.126.
[31] U. Trstenjak, K. Goß, A. Gutsche, J. Jo, M. Wohlgemuth, R.E. Dunin-Borkowski, F. Gunkel, R. Dittmann, Heterogeneous Integration of Graphene and HfO2 Memristors, Adv. Funct. Mater. n/a (n.d.) 2309558. https://doi.org/10.1002/adfm.202309558.
[32] B. Ma, R.D. Rodriguez, A. Ruban, S. Pavlov, E. Sheremet, The correlation between electrical conductivity and second-order Raman modes of laser-reduced graphene oxide, Phys. Chem. Chem. Phys. 21 (2019) 10125–10134. https://doi.org/10.1039/C9CP00093C.
[33] E. Gutiérrez-Pineda, A. Subrati, M.J. Rodríguez-Presa, C.A. Gervasi, S.E. Moya, Electrochemical Exfoliation of Graphene Oxide: Unveiling Structural Properties and Electrochemical Performance, Chem. – Eur. J. 29 (2023) e202302450. https://doi.org/10.1002/chem.202302450.
[34] J.M. Englert, C. Dotzer, G. Yang, M. Schmid, C. Papp, J.M. Gottfried, H.-P. Steinrück, E. Spiecker, F. Hauke, A. Hirsch, Covalent bulk functionalization of graphene, Nat. Chem. 3 (2011) 279–286. https://doi.org/10.1038/nchem.1010.
[35] A.C. Ferrari, J.C. Meyer, V. Scardaci, C. Casiraghi, M. Lazzeri, F. Mauri, S. Piscanec, D. Jiang, K.S. Novoselov, S. Roth, A.K. Geim, Raman Spectrum of Graphene and Graphene Layers, Phys. Rev. Lett. 97 (2006) 187401. https://doi.org/10.1103/PhysRevLett.97.187401.
[36] L.G. Cançado, K. Takai, T. Enoki, M. Endo, Y.A. Kim, H. Mizusaki, A. Jorio, L.N. Coelho, R. Magalhães-Paniago, M.A. Pimenta, General equation for the determination of the crystallite size La of nanographite by Raman spectroscopy, Appl. Phys. Lett. 88 (2006) 163106. https://doi.org/10.1063/1.2196057.
[37] D. Johannsmann, Viscoelastic, mechanical, and dielectric measurements on complex samples with the quartz crystal microbalance, Phys. Chem. Chem. Phys. 10 (2008) 4516–4534. https://doi.org/10.1039/B803960G.

[38] P. Simon, Y. Gogotsi, Materials for electrochemical capacitors, Nat. Mater. 7 (2008) 845–854. https://doi.org/10.1038/nmat2297.
[39] T. Karakoç, H. Ba, L.T. Phuoc, D. Bégin, C. Pham-Huu, S.N. Pronkin, Ultramicroporous N-Doped Activated Carbon Materials for High Performance Supercapacitors, Batteries 9 (2023) 436. https://doi.org/10.3390/batteries9090436.
[40] Y.J. Oh, J.J. Yoo, Y.I. Kim, J.K. Yoon, H.N. Yoon, J.-H. Kim, S.B. Park, Oxygen functional groups and electrochemical capacitive behavior of incompletely reduced graphene oxides as a thin-film electrode of supercapacitor, Electrochimica Acta 116 (2014) 118–128. https://doi.org/10.1016/j.electacta.2013.11.040.
[41] C. Gabrielli, J.J. Garcia-Jareño, M. Keddam, H. Perrot, F. Vicente, Ac-Electrogravimetry Study of Electroactive Thin Films. II. Application to Polypyrrole, J. Phys. Chem. B 106 (2002) 3192–3201. https://doi.org/10.1021/jp013925p.
[42] W. Gao, C. Debiemme-Chouvy, M. Lahcini, H. Perrot, O. Sel, Tuning Charge Storage Properties of Supercapacitive Electrodes Evidenced by In Situ Gravimetric and Viscoelastic Explorations, Anal. Chem. 91 (2019) 2885–2893. https://doi.org/10.1021/acs.analchem.8b04886.
[43] H. Goubaa, F. Escobar-Teran, I. Ressam, W. Gao, A. El Kadib, I.T. Lucas, M. Raihane, M. Lahcini, H. Perrot, O. Sel, Dynamic Resolution of Ion Transfer in Electrochemically Reduced Graphene Oxides Revealed by Electrogravimetric Impedance, J. Phys. Chem. C 121 (2017) 9370–9380. https://doi.org/10.1021/acs.jpcc.7b01421.
[44] Y.-S. Kim, S. Kriegel, K.D. Harris, C. Costentin, B. Limoges, V. Balland, Evidencing Fast, Massive, and Reversible H+ Insertion in Nanostructured TiO2 Electrodes at Neutral pH. Where Do Protons Come From?, J. Phys. Chem. C 121 (2017) 10325–10335. https://doi.org/10.1021/acs.jpcc.7b02395.
[45] J. Agrisuelas, C. Gabrielli, J.J. García-Jareño, H. Perrot, F. Vicente, Kinetic and Mechanistic Aspects of a Poly(o-Toluidine)-Modified Gold Electrode. 2. Alternating Current Electrogravimetry Study in H2SO4 Solutions, J. Phys. Chem. C 116 (2012) 15630–15640. https://doi.org/10.1021/jp303859m.
[46] J. Agrisuelas, C. Gabrielli, J.J. García-Jareño, H. Perrot, F. Vicente, Effects of anion size on the electrochemical behavior of H2SO4-structured poly(o-toluidine) films. An *ac*-electrogravimetry study in acid solutions, Electrochimica Acta 132 (2014) 561–573. https://doi.org/10.1016/j.electacta.2014.04.047.
[47] X. Yang, C. Cheng, Y. Wang, L. Qiu, D. Li, Liquid-Mediated Dense Integration of Graphene Materials for Compact Capacitive Energy Storage, Science 341 (2013) 534–537. https://doi.org/10.1126/science.1239089.
[48] S. Shamaila, A.K.L. Sajjad, A. Iqbal, Modifications in development of graphene oxide synthetic routes, Chem. Eng. J. 294 (2016) 458–477. https://doi.org/10.1016/j.cej.2016.02.109.

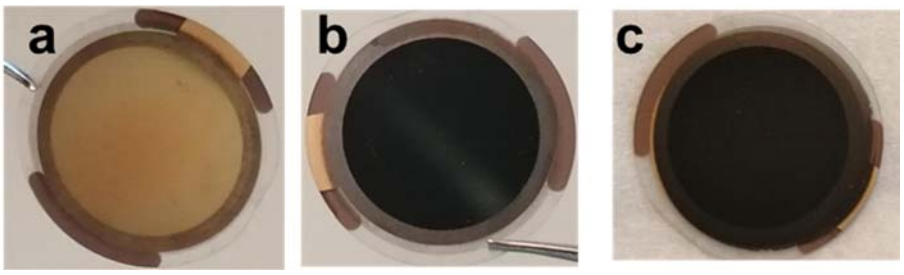

Fig. S1. Photographies of the 5-MHz spray-coated with (a) GO, (b) after the electrochemical reduction of GO leading to ERGO and (c) HyRGO.

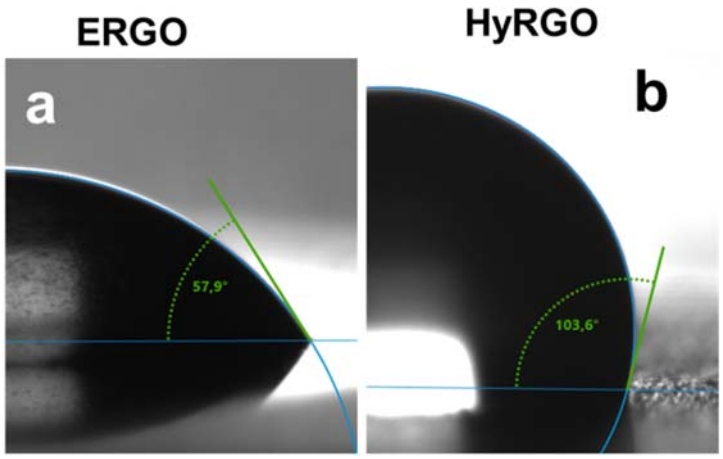

Fig. S2. Contact angle measurements for (a) ERGO and (b) HyRGO.

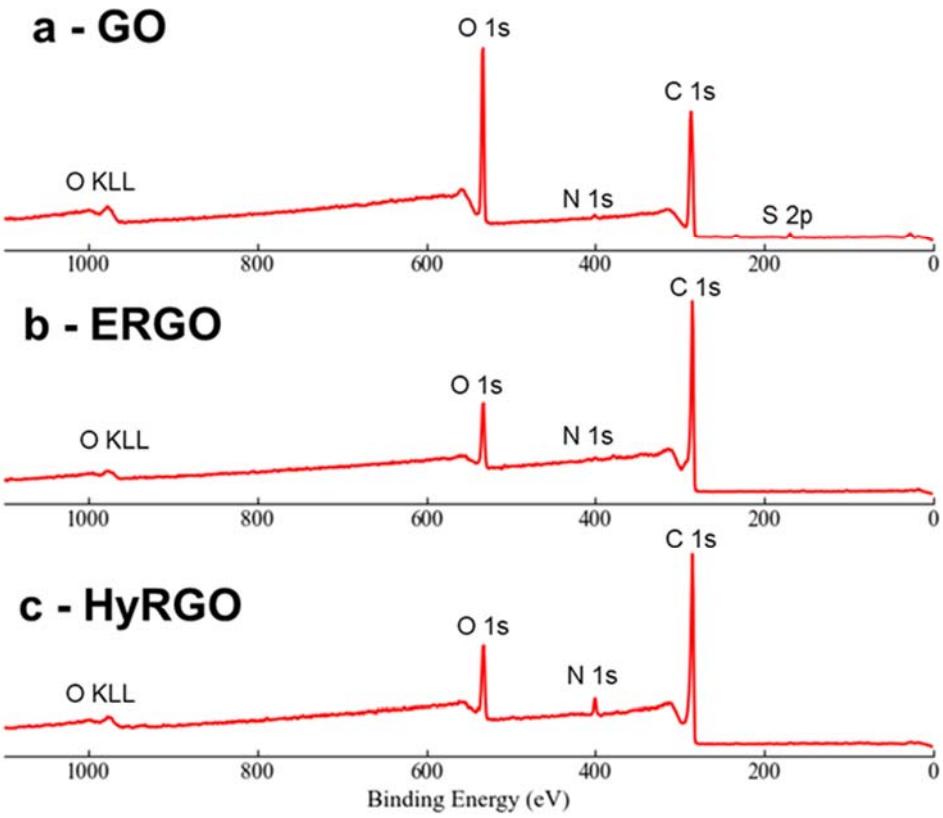

Fig. S3. XPS survey spectra of (a) GO, (b) ERGO and (c) HyRGO.

Table S1. Comparison between the ratio of C=O and C-O between O1s and C1s XPS deconvolutions.

Ratio (C=O – amides)/ (C-O –C-N)	O 1s	C 1s
GO	0.05	0.04
ERGO	0.53	0.52
HyRGO	1.10	0.96

Note S1. Computation of C=O/C-O ratio for HyRGO in Table S1.

These computations allow to deconvolute the contributions of C-N bonds from the C 1s and O 1s spectra, considering that their information are hidden in C 1s C-O contribution for C-N, C 1s and O 1s C=O contribution for O-C=N. They assume that all the N coming in the sample are in amide form because they come from the NMP.

Considering that 3.2 at.% N is present in the sample and 82.4 at.% of C, the ratio between the two is 3.9 at.%. Nitrogen is very probably present as amide functions, as it comes from NMP. This means that every N atom is connected to 3 C atoms, 2 of them by simple bounds C-N and one of them in the amide group, O=C-N. With a ratio N/C of 3.9 at.%, 11.7 at.% of C-N bounds should be found in C 1s spectra, 7.8 at.% of them being simple C-N and 3.9 at.% in amide form. For the computation of C=O/C-O in HyRGO C 1s we used:

$$\frac{C=O\ at.\%}{C-O\ at.\%} = \frac{C=O\ \ (10.7\ at.\%\ from\ C1s)\ \ -\ \ O=C-N\ \ (3.9\ at.\%\ from\ quantification)}{C-O\ (14.9\ \ at.\%\ from\ C1s)\ \ -\ \ C-N\ (7.8\ at.\%\ from\ survey\ spectra)}$$

N/O ratio is 22 at.% from global XPS quantification. Assuming that all the N atoms are in amide groups, this is the theoretical ratio of amide groups to find in O 1s spectra. In the same way as C 1s, C=O/C-O ratio in HyRGO O 1s was computed through:

$$\frac{C=O\ at.\%}{C-O\ at.\%} = \frac{C=O\ \ (62.8\ at.\%\ from\ O1s)\ \ -\ \ O=C-N\ \ (22\ at.\%\ from\ quantification)}{C-O\ (37.2\ at.\%\ from\ O1s)}$$

Table S2. Peak positions used for the deconvolution of O1s and C1s spectra.

C1s, eV Pos. / FWHM	C=C	C-C, C-H	C-O / C-N	C=O	O-C=O	pi-pi
GO	-	285.02 / 1.30	287.19 / 1.30	-	289.00/ 1.30	-
ERGO	284.49 / 0.88	285.02 / 1.70	286.50 / 1.70	288.30 / 1.70	-	290.18 / 2.50
HyRGO	284.43 / 0.86	285.08 / 1.70	286.10 / 1.70	288.06 / 1.70	-	290.85 / 2.60

O1s, eV Pos. / FWHM	C=O	C-O	O-C=O
GO	533.35 / 1.67		532.05 / 1.67
ERGO	532.73 / 2.00	534.13 / 2.00	
HyRGO	532.55 / 1.95	534.27 / 1.95	

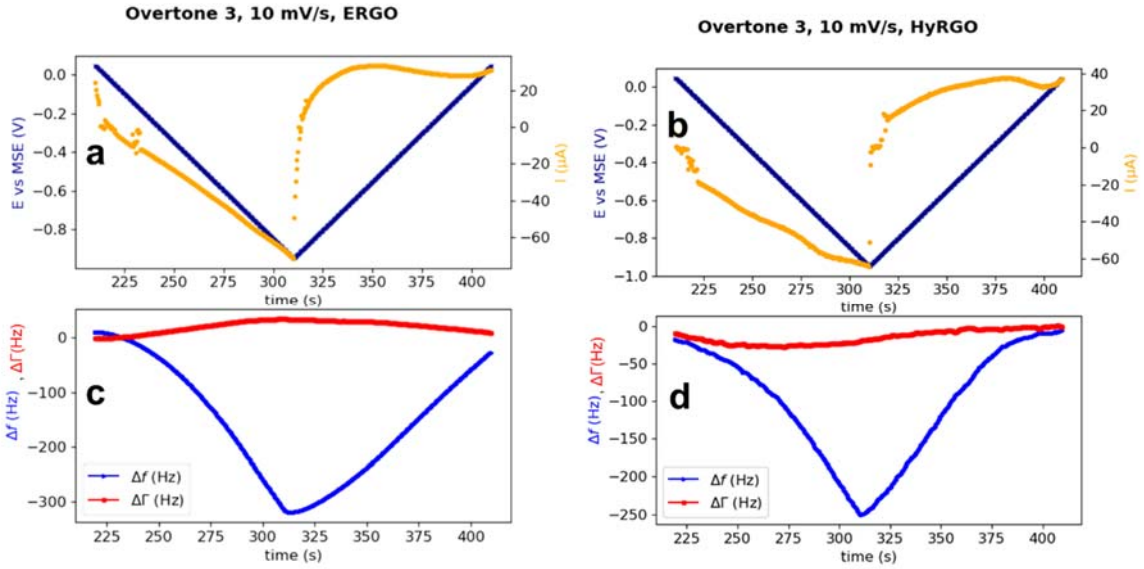

Fig. S4. EQCM with frequency and half width at half maximum (HWHM, Γ) measured for ERGO (a,c) and HyRGO (b,d). (a-b) Current (yellow) and E (blue) and (c-d) Δf (blue) and ΔΓ (red) vs. time. CV is performed in Na_2SO_4 0.5 M at 10 $mV \cdot s^{-1}$

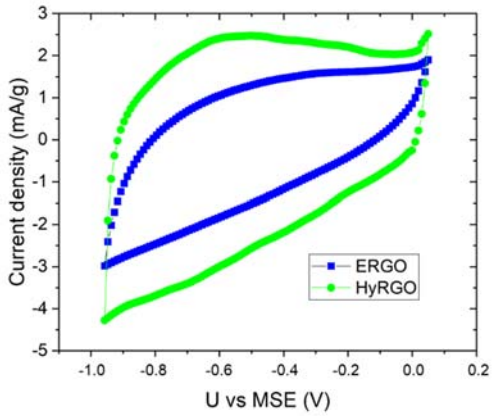

Fig. S5. Cyclic voltammograms at 50 $mV \cdot s^{-1}$ of ERGO and HyRGO in 0.5 M Na_2SO_4

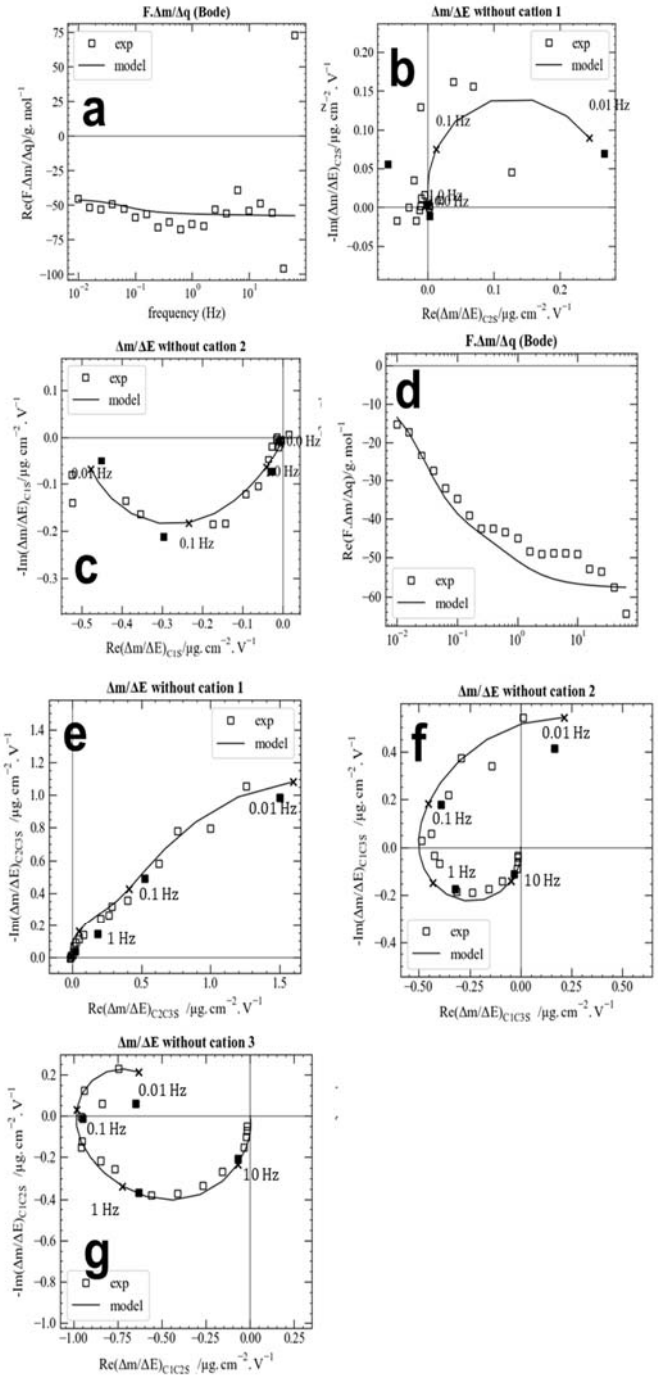

Fig. S6. Complete dataset for the fitting of (a-d) ERGO and (d-g) HyRGO at -0.5 V vs MSE. For ERGO, cation 1 is $Na^+.2H_2O$ with $K_{c1}=3.14\cdot10^{-5}$ cm.s^{-1}, $G_{c1}=6.28\cdot10^{-9}$ mol.cm^{-2}.s^{-1}.V^{-1}, cation 2 is Na^+, with $K_{c2}=6.28\cdot10^{-6}$ cm.s^{-1}, $G_{c2}=5.65\cdot10^{-9}$ mol.cm^{-2}.s^{-1}.V^{-1}, solvent is H_2O with $K_s=9.42\cdot10^{-6}$ cm.s^{-1}, $G_s=9.42\cdot10^{-9}$ mol.cm^{-2}.s^{-1}.V^{-1}. For HyRGO, cation 1 is $Na^+.2H_2O$ with $K_{c1}=5.57\cdot10^{-4}$ cm.s^{-1}, $G_{c1}=4.45\cdot10^{-7}$ mol.cm^{-2}.s^{-1}.V^{-1}, cation 2 is Na^+, with $K_{c2}=4.33\cdot10^{-5}$ cm.s^{-1}, $G_{c2}=2.17\cdot10^{-8}$ mol.cm^{-2}.s^{-1}.V^{-1}, cation 3 is H^+ with $K_{c3}=1.24\cdot10^{-6}$ cm.s^{-1}, $G_{c3}=2.17\cdot10^{-9}$ mol.cm^{-2}.s^{-1}.V^{-1}, and solvent is water with $K_s=3.71\cdot10^{-6}$ cm.s^{-1}, $G_s=-5.57\cdot10^{-9}$ mol.cm^{-2}.s^{-1}.V^{-1}.

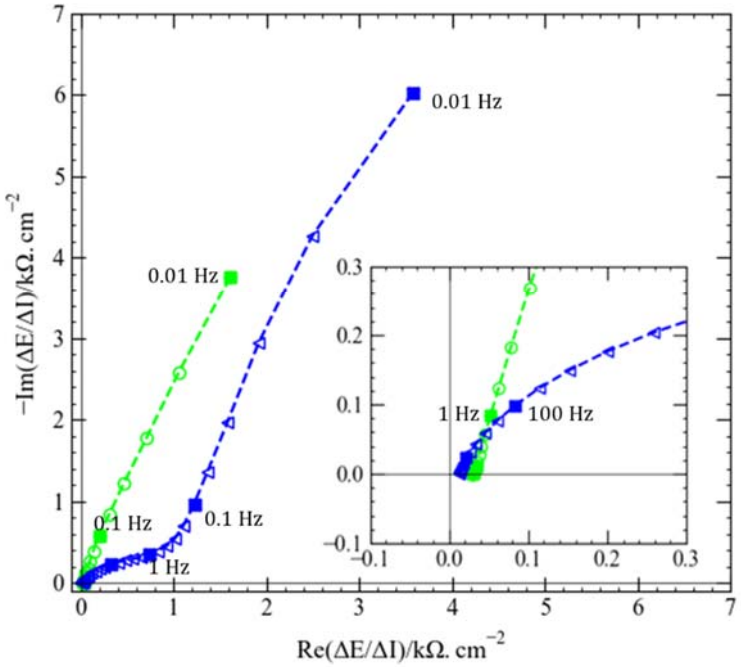

Fig. S7. EIS experimental and theoretical curves and a zoom at higher frequency portion of the Nyquist plot for ERGO (blue) and HyRGO (green) in 0.5 M Na_2SO_4.

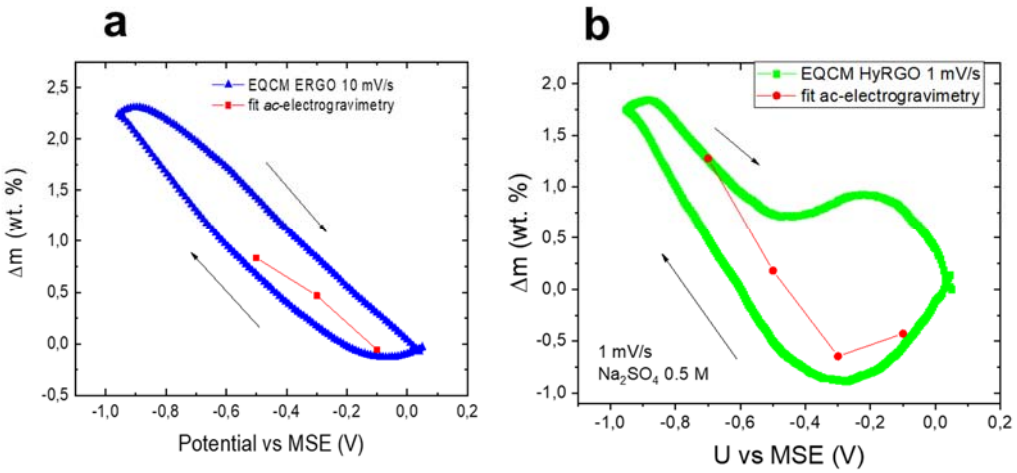

Fig. S8. Experimental Δm (wt. %) curves from EQCM and the reconstructed total mass response using *ac*-electrogravimetry results for (a) ERGO and (b) HyRGO.

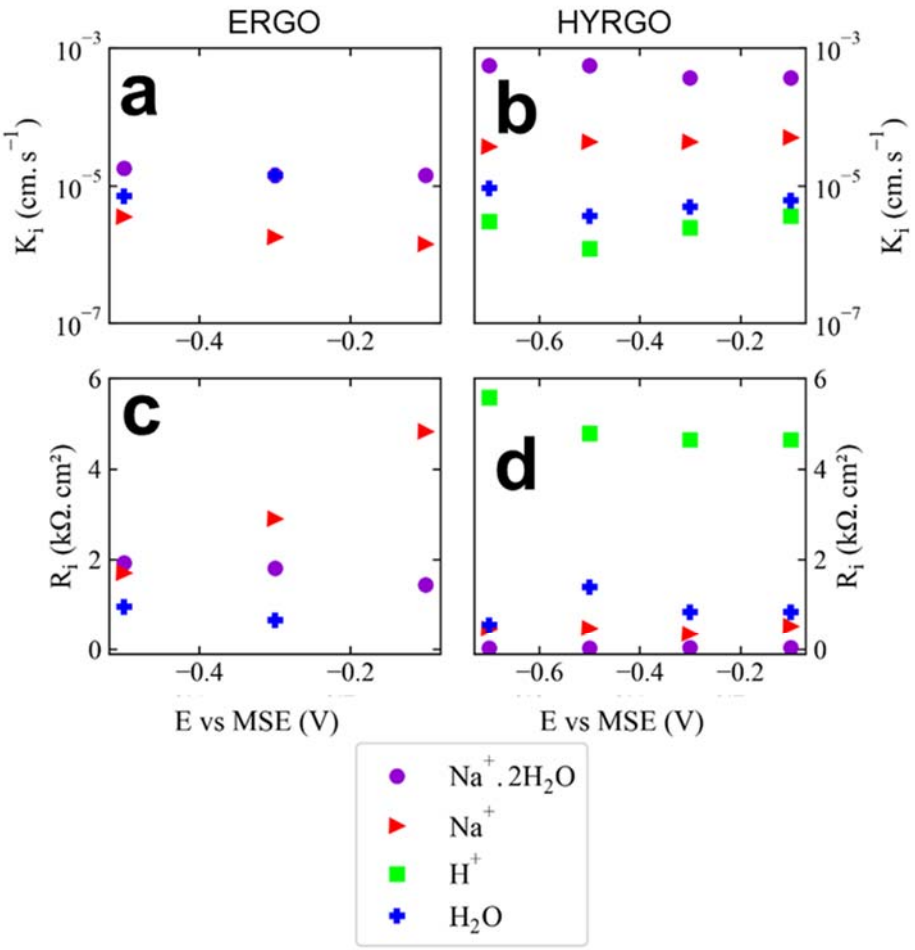

Fig. S9. Evolution of K_i and R_i parameters as a function of the applied potential. For (a,c) ERGO and (b,d) HyRGO.